Composites Part A 134 (2020) 105892

Contents lists available at ScienceDirect

Composites Part A

journal homepage: www.elsevier.com/locate/compositesa

Improving mode II fracture toughness of secondary bonded joints using laser patterning of adherends

A. Wagih, R. Tao, A. Yudhanto, G. Lubineau*

King Abdullah University of Science and Technology (KAUST), Physical Science and Engineering Division, COHMAS Laboratory, Thuwal 23955-6900, Saudi Arabia

ARTICLE INFO

Keywords:
A. Polymer-matrix composites (PMCs)
B. Fracture toughness
C. Damage mechanics
D. Non-destructive testing
CO_2 Laser patterning

ABSTRACT

We improve mode II fracture toughness of secondary bonded joints based on the laser treatment of adherend surfaces. We applied CO_2 Laser treatment to adherend surface alternatively with low and high energy, resulting in a repeated pattern of rough and smooth surfaces. We used ENF test to characterize mode II fracture toughness, G_{II}, of the bonded CFRP substrates. The results demonstrated that our proposed pattern arrested the crack propagation and triggered new damage mechanisms, such as adhesive cracking, adhesive failure and crack migration to the other interface. These additional mechanisms, some of them were non-local in nature, resulted in higher energy dissipation during propagation and, improved G_{II} compared to joints with uniformly-treated adherends. The improvement in G_{II} was dependent on the pattern morphology and reached up to 60%. The proposed strategy worked well for both thin and thick adhesives, and thus could be applied in aerospace and civil structures.

1. Introduction

Large composite structures, such as a fuselage, are generally made by joining smaller parts that are manufactured separately [1]. Mechanical fastening (rivet), welding (fusion bonding) [2] and adhesive bonding are common joining methods. Mechanical fastening involves a machining process and the drilling of a large number of holes on composite parts, which might introduce damage such as matrix cracks and delamination. These damage modes may consequently reduce the load-carrying capacity of the structure, thus requiring extra material that increases the final structural weight [3]. Adhesively bonded joints, where two cured composite adherends are bonded with an adhesive, are increasingly used as an alternative to mechanical joints because the stress concentration typically induced by the fasteners can be alleviated, while the strength-to-weight ratio and damage tolerance can be improved [4]. However, the mechanical performance of a bonded joint is very sensitive to the surface preparation of adherends prior to the bonding process [5]. Poor surface preparation of the adherends generally causes a catastrophic failure (cracks propagate very rapidly once they are initiated), originating from a relatively low toughness of the adhesive-adherend interface.

Several surface preparation methods, including sanding, grit blasting and peel-ply [6–8], have been applied to improve adherend-adhesive interface toughness. Sanding and grit blasting are effective for increasing the adherend surface roughness and removing contaminants from the surface, resulting in better bonding and higher joint strength. However, since both methods are manually operated, the strength of the produced joints varies widely, reducing confidence in the reliability of the joint. Moreover, both techniques are not environmentally friendly because they produce contaminants (dust, debris and particles), which are dangerous when operating with carbon fiber reinforced composites. Additionally, sanding and grit blasting might induce fiber damage, which negatively affects the joint strength [9]. On the other hand, peel-ply is used to overcome the disadvantages of sanding and grit blasting methods, and produces a more consistent surface roughness. However, the peel-ply technique is required to be applied before curing the laminate, which apparently makes it less applicable for large structures and produces chemical contaminants that negatively affect the interface toughness [7].

Various other techniques have been proposed to improve the adhesive-adherend interfacial toughness and avoid catastrophic failure of bonded joints, including adherends in mold corrugation [10,11], z-pinning and stitching [12–15], improved resin properties using different additives [16,17] and thermoplastic inclusions [18,19]. Mold corrugation is efficient for interface toughness improvement; however, it requires the molding of CFRP in a special mold during lamination, which is not an easy task due to the formation of a resin rich area at the corners of the corrugation. Z-pinning and stitching are applicable for

* Corresponding author.
E-mail address: gilles.lubineau@kaust.edu.sa (G. Lubineau).

https://doi.org/10.1016/j.compositesa.2020.105892
Received 3 February 2020; Received in revised form 18 March 2020; Accepted 28 March 2020
Available online 05 April 2020

co-curing process; however, application to the secondary bonding could create fiber rupture. Additionally, z-pinning or stitching creates fiber waviness of principal fibers [15], reducing in-plane strength and stiffness [12]. Energetic techniques such as femtosecond, UV and CO_2 laser treatments are being increasingly employed in adherend surface preparation [20,21]. The acceptance of these techniques has increased recently because they are easily automated methods and eco-friendly [22–24]. Our previous works demonstrated the effectiveness of CO_2 laser treatment for generating extrinsic damage mechanisms, which improves mode I fracture toughness [24,23].

The efficiency of the aforementioned techniques is mostly assessed by studying the improvement of mode I fracture toughness (G_{Ic}), measured using the double cantilever beam test. However, bonded joints are also susceptible to mode II (G_{IIc}) and mixed mode load cases. Due to the difficulty in generating stable delamination growth in mode II, G_{IIc} has been reported on much less in the literature, limiting its availability for analysis. For example, an estimated value of G_{IIc}/G_{Ic} is typically assumed to be 2 in FE analysis [25]. Moreover, a single value of G_{II} measured for a certain adhesive thickness is also used for designing joints with different adhesive thicknesses [26]. These assumptions are rather simplistic due to the fact that G_{IIc}/G_{Ic} values for carbon/epoxy bonded joints may vary from 2.0 to 22.6, while the G_{IIc} value is also highly dependent on adhesive thickness (see Table 1). Therefore, measuring G_{IIc} and studying the effect of the adhesive thickness are of paramount importance when designing new bonded joints. Nevertheless, the measurement of mode II fracture toughness for carbon/epoxy bonded joints is available in terms of data reduction methods for various testing procedures [27–29], construction of R-curve, and cohesive law and FE simulation using cohesive zone modeling [20,30,31]. However, no new methods for improving Mode II fracture toughness in secondary bonded joints have been proposed with deep understanding of energy dissipation mechanisms and the interactions of damage modes.

This paper presents a novel strategy based on CO_2 laser treatment patterning of adherend surfaces to activate new dissipation damage mechanisms that improve mode II fracture toughness. We apply alternating CO_2 laser treatments with low- and high-energy levels representing laser cleaning (LC) and laser ablation (LA), respectively, to the adherend surfaces resulting in a repetitive pattern of rough and smooth surfaces. We perform the End-Notched Flexural (ENF) test using 3-point bending setup to obtain G_{IIc} bonded CFRP substrates. We use two data reduction methods based on simple and Timoshenko beam theories to characterize G_{IIc}. We asses the mechanism of internal damage based on X-ray micro-computed tomography (μ-CT) for identifying different energy dissipation mechanisms. We then correlate the μ-CT micrographs with load-displacement curves, enabling the construction of schematic diagrams of the damage sequence in the adhesive bonded joints with laser-patterned adherend surfaces. We study the effect of adhesive thickness by preparing bonded joint specimens with two adhesive thicknesses, i.e. 0.2 and 0.8 mm, to represent thin and thick adhesive bondlines, respectively, which are typically used in aerospace or civil structures.

2. Experiments and methods

2.1. Specimen preparation

The adherends were manufactured using a unidirectional (UD) tape prepreg carbon/epoxy (T700/M21 Hexply, Hexcel) with fiber volume fraction of 60.8 %. The laminate was composed of eight UD plies $[0°]_8$ with 0.25 mm ply thickness, resulting in a total thickness of 2 mm. 300 × 300 mm^2 panels were manufactured using hand lay up technique and cured using compression molding process. The compression molding process was applied using a hydraulic hot plate press machine at 7 bar pressure and dwell time of 2 h at 180 °C. The heating and cooling rates were kept constant at 3 °C/min. The laminates were cured over a peel-ply layer to produce a rough surface. The elastic ply properties were characterized following ASTM standards and reported as: E_{11} = 135 ± 6 GPa for the longitudinal modulus of elasticity; E_{22} = 8.75 ± 0.27 GPa for the transverse modulus; G_{12} = 4.93 ± 0.14 GPa for the in-plane shear modulus; ν_{12} = 0.29 ± 0.01 for the longitudinal Poisson's ratio.

The adherends of the ENF specimen were cut from the panel using an abrasive water jet machine. The edges of the panels were trimmed and each panel was divided into sub-panels of 260 × 90 mm^2, with the major dimension being aligned with 0°. We treated the panels using a CO_2 laser, which will be described in the next section. After the laser treatment, adherends were submerged into acetone for 10 min in sonicator, dried at 60°C for 30 min and cleaned using compressed air to remove any contaminants on adherend's surfaces. We bonded two sub-panels were bonded using epoxy adhesive (Araldite 420 A/B, Huntsman; strength = 36 MPa; modulus = 1.5 GPa). Two types of ENF specimen were prepared depending on the adhesive thickness, i.e. 0.8 mm and 0.2 mm thickness. After bonding, samples are cured at 60°C for 3 h and kept 24 h at room temperature. A pre-crack length a_d of 5 mm was made by inserting a nonadhesive polyethylene of 18 μm thickness in order to avoid unstable crack initiation. Finally, bonded sub-panels were cut into three samples each of 25 mm width and 260 mm length to fit the ENF samples requirement.

2.2. Laser patterning for adherend

Prior to bonding, the CO_2 laser treatment was applied to the composite adherends to generate a predefined surface patterning. The patterns on the adherend surface were created to arrest the crack propagation at the adherend-adhesive interface (local energy dissipation) and to trigger other energy dissipation mechanisms inside the adhesive layer. Some of these mechanisms, as will be demonstrated later, appeared to be non-local, allowing us to exploit the dissipative properties of the adhesive layer. To this end, we subjected the adherend surface (that has a peel-ply texture) to the laser treatment using CO_2 pulsed laser irradiation (λ = 10.6 μm, PLS6.75 Laser Platform, Universal Laser Systems, NY, USA). Two laser treatment approaches were employed, namely laser cleaning (*LC*) and laser ablation (*LA*), alternatively to apply the pattern. In previous studies [24,23], *LC*, whose fluence was F_p = 1.2 J/cm², the authors achieved a slightly cleaner surface without modifications to the surface roughness. On the other hand, *LA* employed a higher pulse fluence, F_p = 3.6 J/cm², and fully removed the surface resin and exposed carbon fibers. The processing parameters of *LA* and *LC* are listed in Table 2. Fig. 1 shows the laser patterning with

Table 1
G_{Ic} and G_{IIc} for different adhesively bonded joints available in the literature.

Adhesive material	Adhesive thickness (mm)	G_{Ic} (N/mm)	G_{IIc} (N/mm)	G_{IIc}/G_{Ic}
Epoxy (AV138) [26,32]	0.5	4.91	14.2	2.9
Epoxy (Araldite 2015) [26]	0.2	–	7.22	–
Epoxy (Araldite 2015) [26]	0.5	0.53	11.9	22.6
Epoxy (Araldite 2015) [26]	1	–	21.1	–
Epoxy (Araldite 2015) [33]	0.2	0.43	4.70	10.9

Table 2
CO_2 laser processing parameters used for laser cleaning (LC) and laser ablation (LA).

Parameters	Surface pretreatments	
	LC	*LA*
Laser wavelength (μm)	10.6	10.6
Focal distance (mm)	50	50
Spot diameter (μm)	200	200
Laser speed (mm/s)	500	500
Pulse frequency (kHz)	20	20
Processing gas (–)	Air	Air
Average power (W)	7.5	22.5
Pulse fluence (J/cm^2)	1.2	3.6

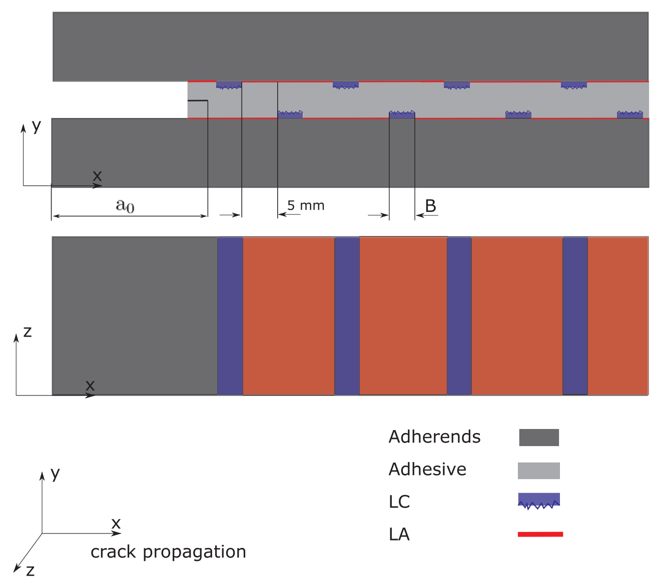

Fig. 1. Schematic representation of the bonded joint with the proposed laser patterning. (For interpretation of the references to colour in this figure legend, the reader is referred to the web version of this article.)

different width of *LC* treatment, B = 2.5, 5.0 and 10.0 mm. We kept the distance between *LC* treatment in upper and lower adherends constant of 5 mm, as shown in Fig. 1.

The main parameter guiding the efficiency of the laser irradiation process is the pulse fluence (F_p):

Table 3
Test matrix of the end-notch flexure.

Label	Treatment	LC-treated width (mm)	Adhesive thickness (mm)
LA-T008	*LA*	–	0.8
LA-T002	*LA*	–	0.2
LC-T008	*LC*	–	0.8
P250-T008	*LA* + *LC*	2.5	0.8
P500-T008	*LA* + *LC*	5.0	0.8
P500-T002	*LA* + *LC*	5.0	0.2
P1000-T008	*LA* + *LC*	10.0	0.8

$$F_p = I_p \cdot t_p = \frac{W_{ave}}{f \cdot A_s} = \frac{4W_{ave}}{v \cdot PPI \cdot \pi d^2}, \tag{1}$$

where I_p is the laser irradiance, t_p is the laser pulse duration, v is the traveling speed, *PPI* represents the number of pulses per inch, $f = v \cdot PPI$ is the pulse frequency, W_{ave} is the average pulse power, and $A_s = \pi d^2/4$ is the spot size of the laser. Previous investigations have revealed that the surface morphology and energy varies for different pulse fluence and frequency [24,23]. In the present work, we kept the traveling speed and the number of pulses per inch constant at, $v = 500$ mm/s and $PPI = 1000$, respectively. The focal distance was optimized so that the resulting laser spot diameter d was 200 μm.

2.3. Surface characterization methods

We measured the surface roughness of adherends after laser treatments along the fiber direction using a surface profilometer (Dektak 150 Surface Profiler, Veeco, New York, USA) with a 5 μm-diameter stylus probe. The probing location for the roughness measurement covered *LA*-treated, *LC*-treated and LC-LA transition areas. We performed five measurements for each spot with 9 mm gauge length and 0.1667 μm/point resolution. We used a Field Emission Scanning Electron Microscope (FE-SEM) model Quanta 600 (FEI) with secondary electrons to inspect the surface morphology of the adherend after laser treatments. Prior to SEM observation, the adherend surface was sputtered with Au/Pt layer.

2.4. ENF test

We performed the end-notch flexure (ENF) test based on ASTM D7905 to obtain the mode II interlaminar fracture toughness of the secondary bonded joints. Fig. 2 shows the ENF test setup and schematic representation of the sample under concentrated load P. We used a three-point bending fixture with 10 mm diameter support and 10 mm

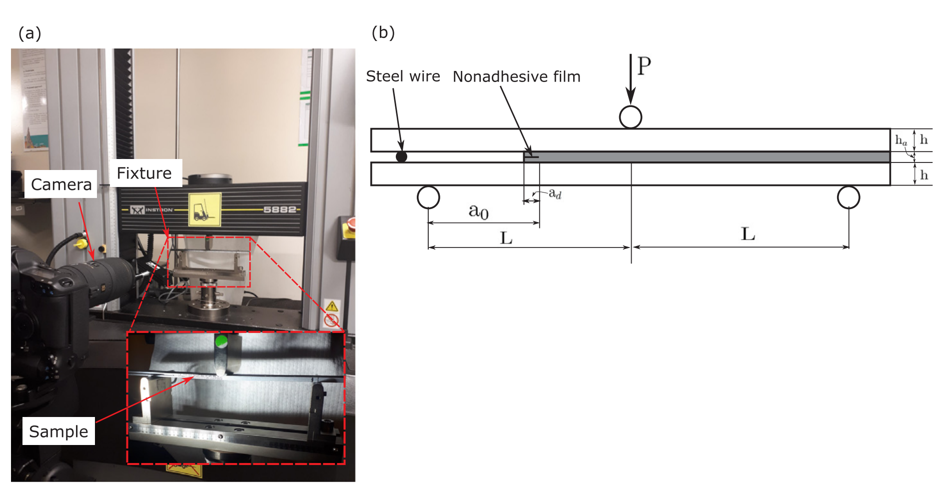

Fig. 2. Experimental test (a) setupand (b) schematic representation of ENF specimen and test geometry. Dimension used in the study were: L = 90 mm, a_0 = 40 mm, a_d = 5 mm and loading roller diameter and supports are 10 mm. (For interpretation of the references to colour in this figure legend, the reader is referred to the web version of this article.)

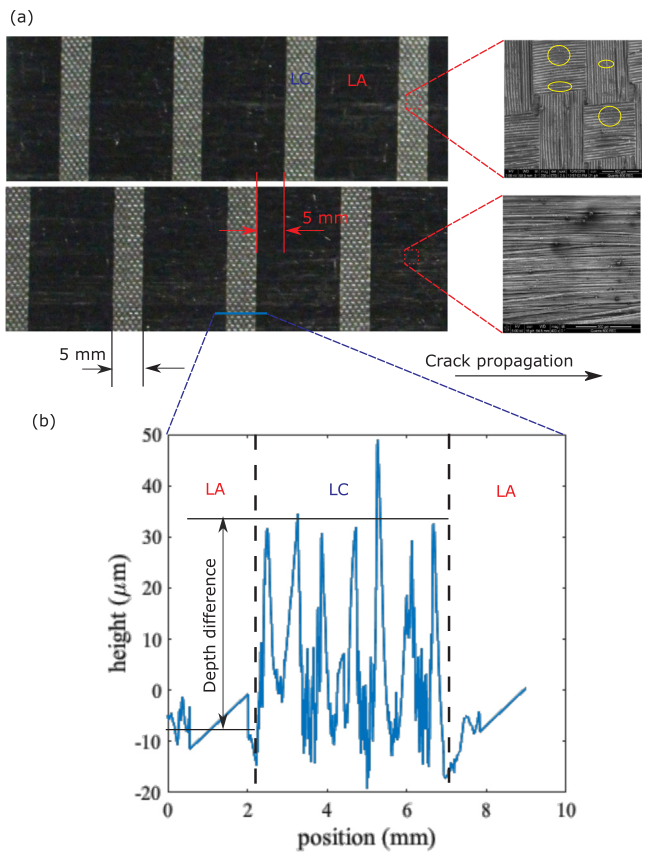

Fig. 3. Adherend's surface characteristics of sample with 5 mm pattern width (a) morphology of the two laser treatments *LA* and *LC* and (b) profile scan of *LC* treatment and transition stage between *LA* and *LC* marked with the blue line in (a). (For interpretation of the references to colour in this figure legend, the reader is referred to the web version of this article.)

diameter indenter. We slightly modified the half-span length (L) and initial crack length (a_0) compared to the ASTM standard to ensure a stable crack propagation [28,34]. The L and a_0 considered in this study were 90 mm and 40 mm, respectively. A steel wire with a diameter equal to the adhesive thickness was inserted between the adherends at the unbonded area to ensure uniform distribution of the compressive stresses during loading [34,20]. A digital camera was used to record the photos of sample edge and crack extension, which were synchronized with the load-displacement data. The ENF test matrix designed to study the effect of laser patterning and adhesive thickness on mode II fracture toughness is shown in Table 3.

2.5. Data reduction methods

We employed two data reduction methods, i.e. Simple Beam Theory (SBT) and Timoshenko Beam Theory (TBT), to compute the evolution of mode II fracture toughness during the ENF test with respect to the crack length (R-curve). Both methods utilized the effective crack length a_e to overcome the difficulties related to monitoring of the crack length during the ENF test [34]. During the tests, the crack tip was not easily identified due to the bending of two arms that are in direct contact, causing a large uncertainty. Moreover, the relatively high ductility of the adhesive (Araldite 420) produces a large Failure Process Zone (FPZ) in front of the crack tip, which contributes to higher energy dissipation. Additionally, a thick adhesive layer increases the size of the FPZ that, eventually contributing to higher energy dissipation. The data reduction methods, which use the effective crack length, take this energy dissipation into account indirectly.

- Simple Beam Theory (SBT)
  Simple beam theory (SBT) is one of the most common methods used to analyze ENF test results. Assuming that the adhesive layer is rigid, the specimen compliance, C, can be calculated using the following expression [35]:

$$C = \frac{\delta}{P} = \frac{3a^3 + 2L^3}{8Bh^3E} \tag{2}$$

δ is applied displacement at the loading point, P is load, a is crack length, L is half span length, B is sample width, h is adherend thickness and E is elastic modulus of the adherend. Eq. (2) was used to replace a with a_e, which is the effective crack length as follows:

$$a_e = \left[\frac{8\delta Bh^3E}{3P} - \frac{2}{3}L^3\right]^{\frac{1}{3}} \tag{3}$$

Then, according to the Irwin-Keis relation in linear elastic fracture mechanics (LEFM), the mode II fracture toughness can be calculated as follows:

$$G_{II} = \frac{P^2}{2B}\frac{dC}{da} \tag{4}$$

The direct relation between G_{II} and a_e can be obtained by substituting Eq. (2) into Eq. (4) as follows:

$$G_{II} = \frac{9P^2a_e^2}{16B^2h^3E} \tag{5}$$

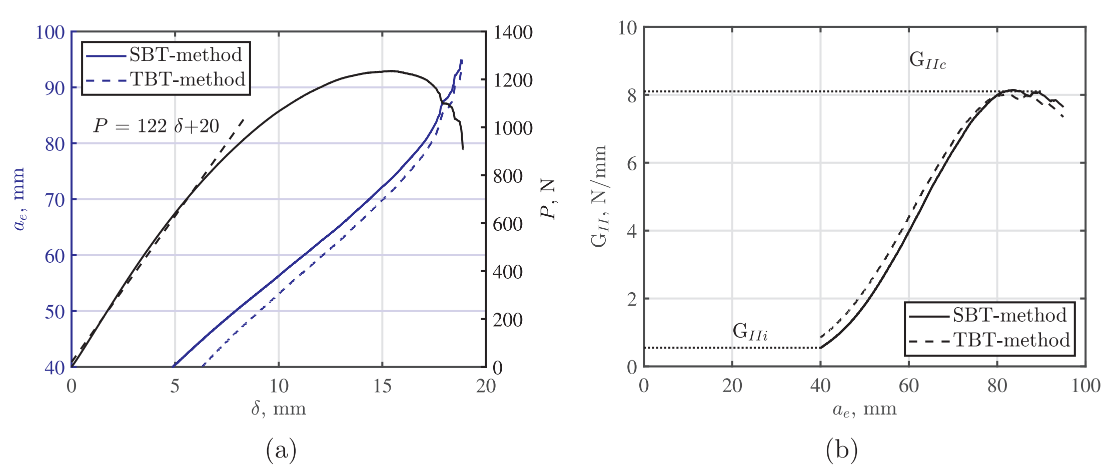

Fig. 4. Example of ENF test response of LA-T008 sample (a) load-displacement effective crack length-displacement curves and (b) R-curve of the same sample computed using SBT and TBT methods. (For interpretation of the references to colour in this figure legend, the reader is referred to the web version of this article.)

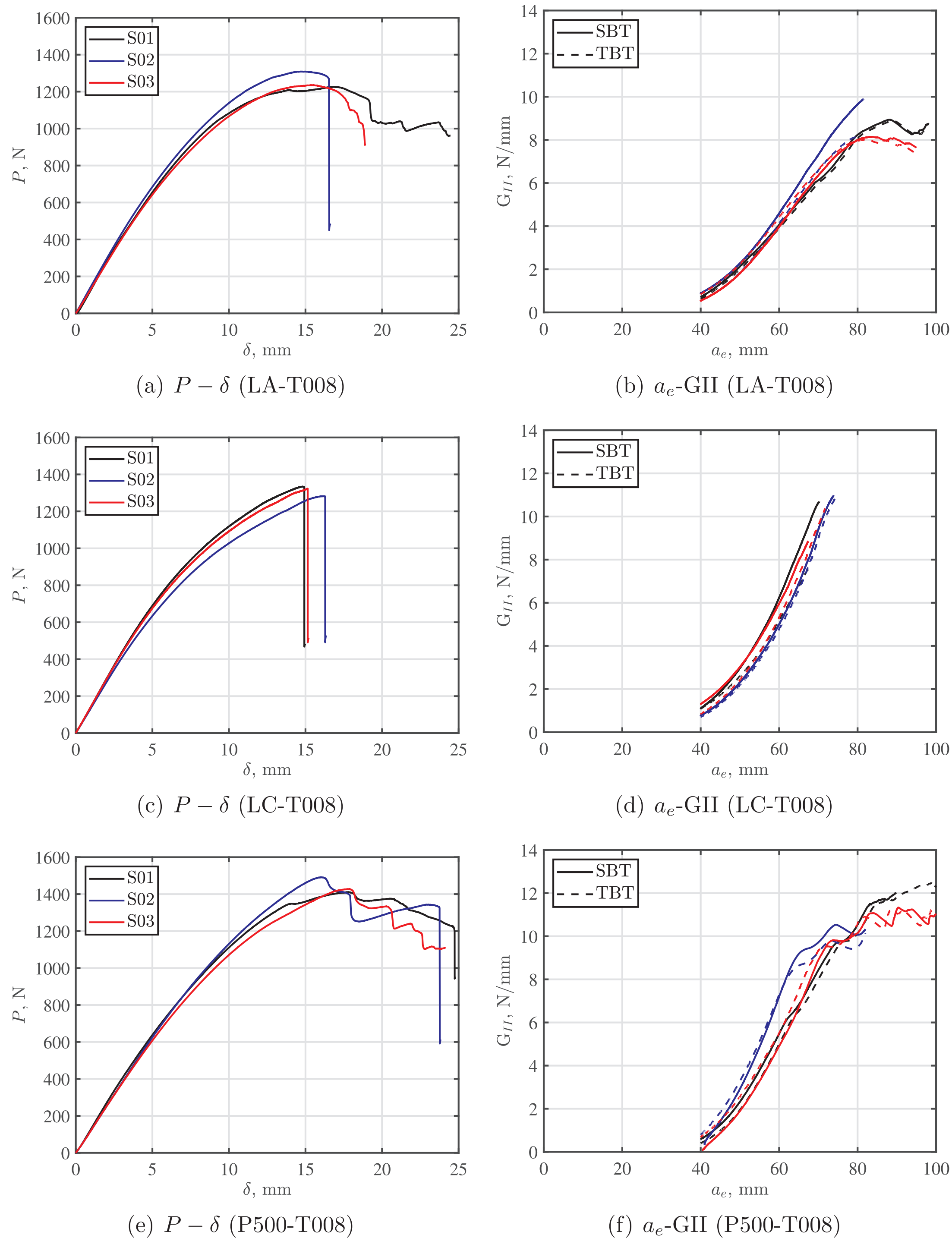

Fig. 5. ENF test response of LA-T008, LC-T008 and P500-T008. The load-displacement response is shown in left hand figures while corresponding R-curves are shown in the right hand figures. (For interpretation of the references to colour in this figure legend, the reader is referred to the web version of this article.)

where E was replaced by E_{11} for composite adherend.

- Timoshenko Beam Theory (TBT)

  In TBT, the specimen compliance is calculated using the following expression [30]:

$$C = \frac{\delta}{P} = \frac{3a^3 + 2L^3}{8Bh^3E_f} + \frac{3L}{10G_{13}Bh} \tag{6}$$

where G_{13} is the adherend flexural modulus and E_f is the equivalent flexural modulus. In Eq. (6), E_f is used instead of E_{11} in order to take into account the effect of the adhesive layer, and the stress concentration at the crack tip and the contact between two adherends. E_f can be calculated using Eq. (6) by substituting the initial crack length a_0 and initial compliance C_0 that were computed at the early stage of loading, which then leads to:

$$E_f = \frac{3a_0^3 + 2L^3}{8Bh^3}\left(C_0 - \frac{3L}{10G_{13}Bh}\right)^{-1} \tag{7}$$

a_e was calculated using Eq. (6). By taking into account E_f, Eq. (7) can be written as a function of specimen compliance as follows:

Table 4
Summary of maximum load, P_{max}, and fracture toughness, G_{IIi} and G_{IIc} for all the tested joints. Note: G_{IIc} of LC-T008 could not be obtained since the crack propagated very quickly causing catastrophic failure.

Label	P_{max}(N)	G_{IIi} (N/mm)		G_{IIc} (N/mm)	
		SBT	TBT	SBT	TBT
LA-T008	1256 ± 55	0.81 ± 0.15	0.55 ± 0.19	8.82 ± 0.81	8.34 ± 0.43
LA-T002	737 ± 68	0.41 ± 0.22	0.35 ± 0.25	2.49 ± 0.30	2.39 ± 0.21
LC-T008	1312 ± 21	1.05 ± 0.24	0.87 ± 0.17	–	–
P250-T008	1345 ± 92	0.71 ± 0.13	0.63 ± 0.35	10.92 ± 0.55	10.64 ± 0.52
P500-T008	1443 ± 76	0.45 ± 0.21	0.58 ± 0.27	11.29 ± 0.76	11.28 ± 1.12
P1000-T008	1560 ± 47	1.02± 0.09	0.84 ± 0.15	14.1 ± 0.40	13.8 ± 0.84
P500-T002	806 ± 87	0.91 ± 0.35	0.84 ± 0.18	3.11 ± 0.44	2.84 ± 0.39

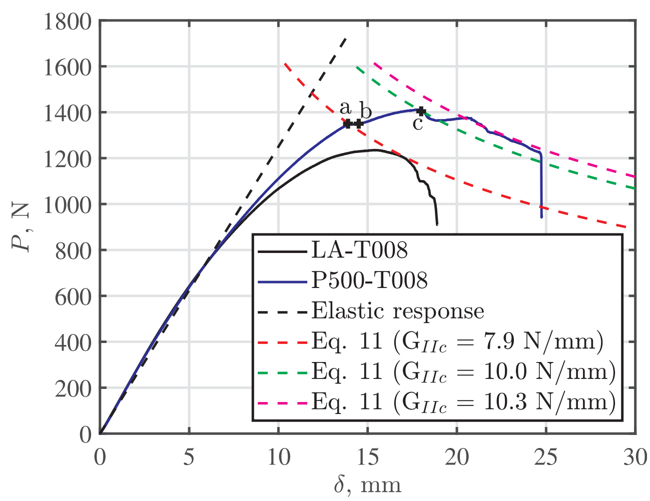

Fig. 6. $P - \delta$ curves representative samples of LA-T008 and P500-T008 configurations. (For interpretation of the references to colour in this figure legend, the reader is referred to the web version of this article.)

$$a_e = \left[\frac{C_c}{C_{0c}}a_0^3 + \frac{2}{3}\left(\frac{C_c}{C_{0c}} - 1\right)L^3\right]^{1/3} \tag{8}$$

where

$$C_c = C - \frac{3L}{10G_{13}Bh};C_{0c} = C_0 - \frac{3L}{10G_{13}Bh} \tag{9}$$

Considering Irwin-Keis relation, Eq. (4), the relation between G_{II} and a_e can be expressed as:

$$G_{II} = \frac{9P^2a_e^2}{16B^2h^3E_f} \tag{10}$$

2.6. Damage identification method

We used the X-ray micro-computed tomography (μ-CT) system (Nikon X-TEK XT-H225) to identify internal damage modes in the tested specimen. Since the two adherends of the specimen were not entirely separated after the test, a 2 mm thick wedge was inserted into the initial crack area to improve damage visualization. The parameters set in μ-CT system were 60 kV voltage, 100 μA intensity, 250 ms exposure time, 11.27 μm voxel size and 26 mm field of view. In all inspected specimens, the machine acquired 2500 projections during the 360° rotation. We reconstructed the images using CT Pro 3D and then analyzed the images using Avizo software.

3. Results

3.1. Surface characteristics of patterned adherend

Fig. 3(a) shows the surface characteristics of the interface with two alternating treatments of *LA* and *LC*. The width of the *LC*-treated strip is 5 mm, while the gap between the two *LC*-treated adherends is also 5 mm. FE-SEM on the right shows that the *LC*-treated strip maintains the morphology of peel ply. The slight removal of epoxy showing bare fibers (see yellow circles) helps to improve the bonding between the adherend and adhesive. On the other hand, the *LA*-treated strip exhibits a full removal of the epoxy from the surface and bare fibers. The surface roughness of *LC* and the transition stage between *LA* and *LC* is shown in Fig. 3(b). The *LC*-treated area shows local peaks with an average amplitude of 33 µm. The *LA*-treated area displays a smooth surface with an average roughness of 8 µm due to the removal of the epoxy. The depth difference (as indicated in Fig. 3(b)) between *LA*- and *LC*-treated roughness is around 40 µm.

3.2. ENF test results

Fig. 4 shows an example of load-displacement ($P - \delta$), effective crack length-displacement ($a_e - \delta$) and mode II fracture toughness-crack length (G_{II}-a_e) behavior (R-curve) of LA-T008 sample obtained using the SBT and TBT methods to highlight some characteristics of the data reduction methods. Fig. 4(a) shows that the SBT method generally produces slightly higher a_e than the TBT method at the same displacement level. Such a difference is originated from the method of defining compliance, and eventually a_e. In the SBT methods, C keeps changing at each increment, while a_e is computed substituting C into Eq. (2). However, the TBT method defines a crack initiation when C is larger than C_0; in this case, C_0 is equal to 1/122 mm/N (inverse of the linear fitting slope in Fig. 4(a)). C_0 is determined by linear fitting of the elastic loading part of $P - \delta$ curve, as shown in Fig. 4(a).

Notably, the a_e computed using both methods is always larger than the real crack length. This is due to nonlinear deformation of the adhesive layer before the crack starts to propagate [34]. The nonlinear deformation dissipates some energy due to plasticity, which is taken into account in both methods to calculate the hypothetical crack [34]. Nonetheless, the R-curve computed using both methods shown in Fig. 4(b) is similar. Two main features can be extracted from this figure: the initiation and propagation fracture toughness, G_{IIi} and G_{IIc}, respectively. The initiation fracture toughness is the fracture toughness at the initial crack length, 40 mm. The fracture toughness increases with increasing crack length until a fairly constant value is achieved, at which the G_{IIc} is defined.

Fig. 5(a, c, e) shows $P - \delta$ obtained from ENF specimens with 0.8 mm adhesive thickness (LA-T008, LC-T008, P500-T008). Fig. 5(b, d, f) shows their corresponding R-curves, which feature a good repeatability. A summary of the maximum load, P_{max}, and fracture toughnesses, G_{IIi} and G_{IIc}, computed using the SBT and TBT methods is shown

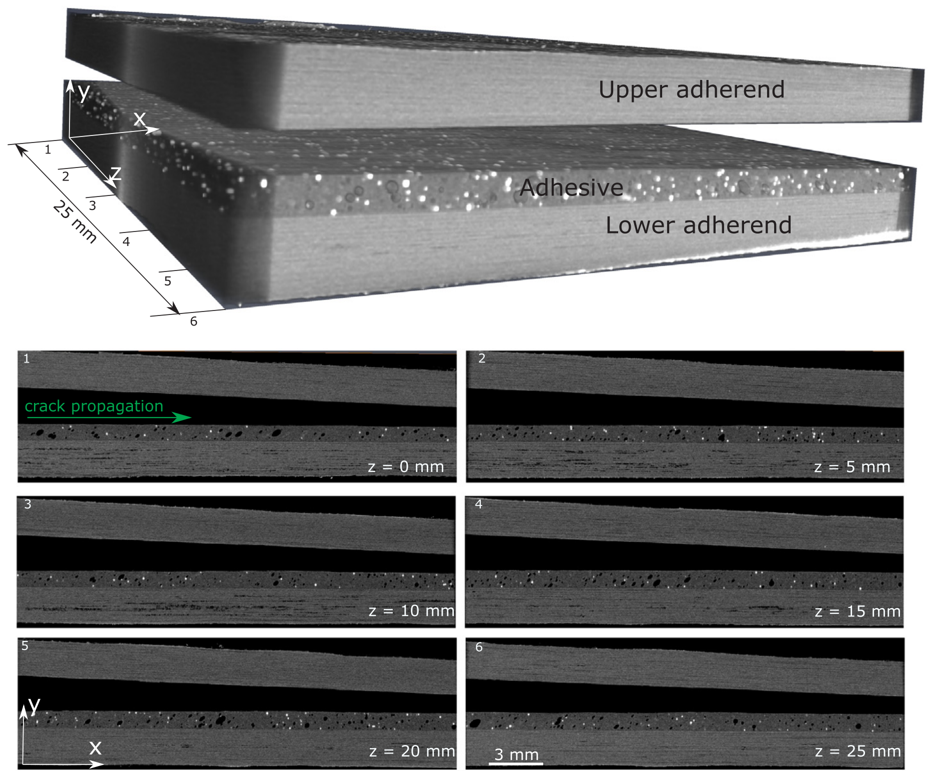

Fig. 7. 3D μ-CT micrographs of LA-T008 sample (the upper figure) and slices through the sample width (the lower 2D micrographs). (For interpretation of the references to colour in this figure legend, the reader is referred to the web version of this article.)

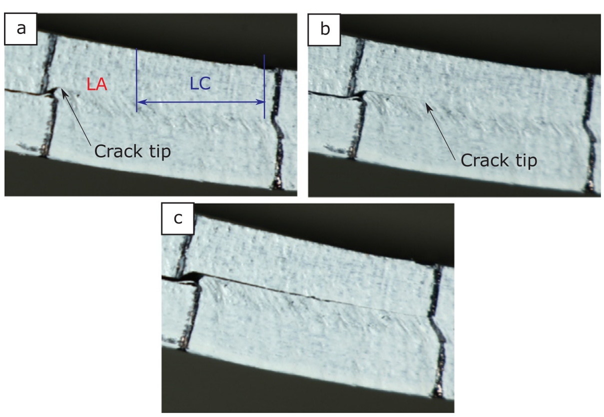

Fig. 8. Photos of P500-T008 sample during test at points a, b and c marked in the $P-\delta$ curve (Fig. 6). (For interpretation of the references to colour in this figure legend, the reader is referred to the web version of this article.)

in Table 4.

4. Discussion

4.1. Energy dissipation mechanisms

Fig. 6 shows $P-\delta$ curves of representative samples of LA-T008 and P500-T008 along with four dash lines estimated from the theory. The black-coloured dashed line represents the initial elastic response. Three non-linear dashed curves represent theoretical $P-\delta$ responses during crack propagation, which are calculated based on Allix et al. [36] as follows:

$$\delta = \frac{8PL^3}{384EI} + \frac{16\sqrt{EI}}{P^2}\left(\frac{BG_{IIc}}{3}\right)^{1.5} \quad (11)$$

E is the in-plane elastic modulus, I is the second moment of area. Each of these dashed curves corresponds to a special value of G_{IIc} as explained in the following.

We observed different mechanisms of degradation and of energy dissipation between the non-patterned and patterned samples. For the non-patterned samples (e.g. LA-T008), 3D reconstructed μ-CT image and the corresponding slices shown in Fig. 7 suggest that the dissipation mechanism under mode II is purely interfacial (cohesive failure). By observing the experimental curves for LA-T008 (solid black curve on Fig. 6), we notice first an elastic response, followed by the progressive establishment of a process zone so that the curve finally reaches the red dashed curves, which corresponds to the theoretical curves for crack propagation with $G_{IIc} = 7.9N/mm$. This is consistent with the value obtained in Table 4. The value of G_{IIc} substituted in Eq. (11) is slightly lower than the experimental value due to the plastic deformation of the adhesive layer, which is not considered in the Allix et al. [36] model. We then observe the propagation of a pure interfacial crack followed by catastrophic failure.

On the contrary, for the laser-patterned specimen (e.g. P500-T008), we observed different mechanisms of degradation. As indicated by the experimental curves for P500-T008 (solid blue curve on Fig. 6), we also notice the same elastic response and the softening due to the development of a process zone until Point “a”. Point “a” corresponds to a crack initiation at the LA-treated interface (see Fig. 8(a)). Between Point “a” and Point “b”, the crack mainly propagates in an interfacial manner along the LA-treated interface (see Fig. 8(b)), which is reflected in a slight load reduction from “a” to “b”. As expected, the $P-\delta$ curve follows the red dashed line at that stage (G_{IIc} = 7.9 N/mm), similar to the LA-T008 behavior. At Point “b”, the crack reaches the LC-treated interface.

The propagation continues along the LC interface from Point “b” to Point “c”, but at a lower rate because different mechanism are being activated (see Fig. 8(c)). Crack propagation from “b” to “c” is arrested due to the change in surface morphology (see Fig. 3) and and the good

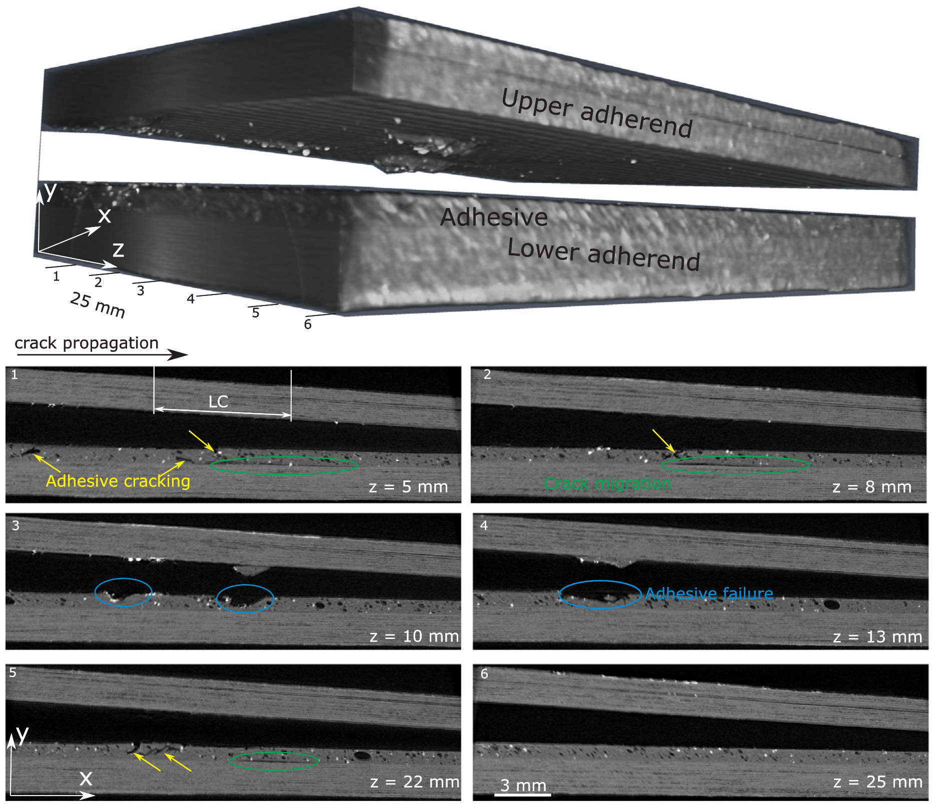

Fig. 9. 3D μ-CT micrographs of P500-T008 sample (the upper figure) and slices through the sample width (the lower 2D micrographs). (For interpretation of the references to colour in this figure legend, the reader is referred to the web version of this article.)

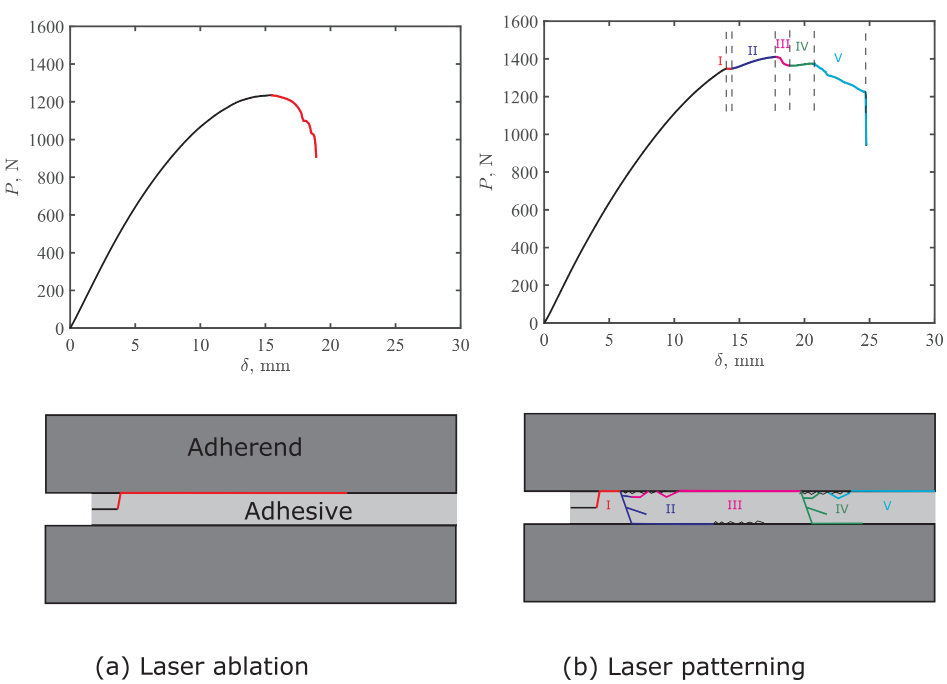

Fig. 10. Schematic representation of damage sequence in adhesive bonded joints with (a) non-patterned laser ablation and (b) patterned adherend surface (each color in the load displacement curve refers to the corresponding damage in the schematic drawing). (For interpretation of the references to colour in this figure legend, the reader is referred to the web version of this article.)

adhesion between the adherend and adhesive activated by the peel-ply treated surface [37] (we recall that the morphology of the surface created by the peel-ply is preserved during the LC treatment; see Fig. 3(a)). Fig. 9 shows the 3D μ-CT micrograph and 2D slices across the width of the P500-T800 specimen. In the 2D slices, we identified the damage types that occurred due to patterning,.ie., the creation of secondary cracks and fragmentation of the adhesive layer, crack migration to the lower adherend's interface and crack propagation in the upper adherend's interface. The interplay between these damage mechanisms results in dissipating extra energy during the mode II fracture process, which eventually increases mode II fracture toughness. Despite the common difficulty encountered in assessing mode II crack propagation, we found that observing crack propagation from the specimen edges using a digital camera and studying the internal damage using micro-computed tomography were useful for elucidating the detailed dissipation mechanisms. It is valuable highlighting that the visual

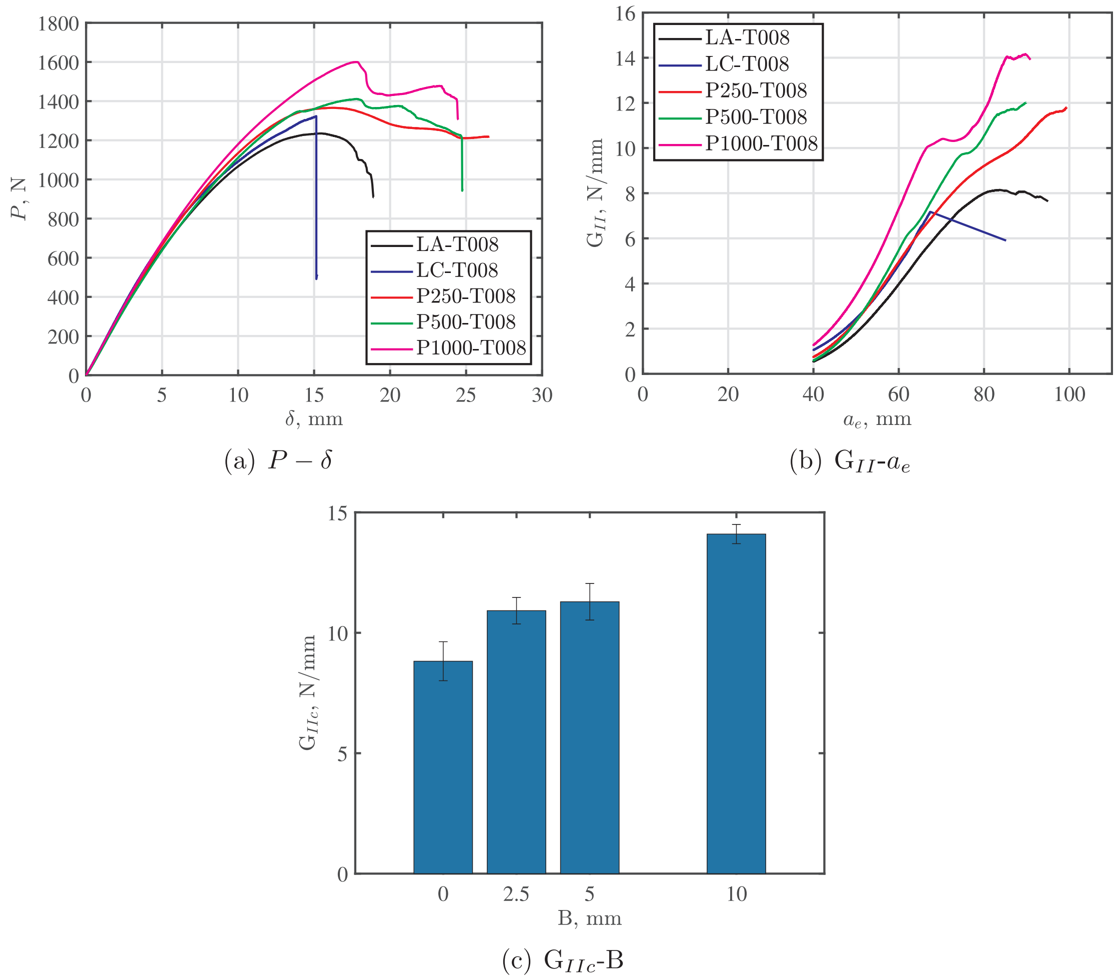

Fig. 11. Effect of *LC* laser treatment width on the ENF test response. G_{II} and G_{IIc} in (b) and (c), are plotted based on SBT method calculations. (For interpretation of the references to colour in this figure legend, the reader is referred to the web version of this article.)

inspection of the samples after testing does not show any of these three internal damage mechanisms (see Fig. 8 and 9 z = 25 mm). This observation highlights the importance of performing μ-CT inspections for ENF test samples, especially when we expect mode II fracture toughness improvement.

At Point “c”, the crack has fully crossed the patterned area and starts again to propagate along the LA-treated interface again. A load drop occurs in the load displacement curve due to the quick propagation of the crack. The green-dashed curve corresponds to the Eq. (11) prediction with G_{IIc} = 10.1 N/mm. This identified value means that the dissipation remains high (theoretically, after point “c”, the load should be reduced to follow the red line again) even if the crack is back at the LA-treated interface. This high dissipation can be explained by the interlocking effect of the fragments (Fig. 9) that have been created during the propagation in the patterned area, which increases the performance of the joint. Then, since the pattern is repeated, the crack is arrested again, creating an increased load to the fit with the purple line, which is the prediction of Eq. (11) considering G_{IIc} = 10.3 N/mm and hence, the higher fracture energy.

It is valuable noting that the propagation of the aforementioned damage mechanisms not only improves fracture toughness but also helps to improve the joint flexural strength, as shown in Table 4 by the maximum load. The growth of these damage mechanisms and the interaction between them, redistributes the exerted shear and normal stresses due to bending, which improves the flexural strength of the joint. The patterned interface then results in higher strength and toughness than the LA-treated and LC-treated interfaces taken separately. The sequence of mechanisms and differences between homogeneous and patterned interfaces have been summarized for clarity in Fig. 10.

4.2. Effect of laser patterning width

Fig. 11 shows that the improvement of mode II responses ($P - \delta$ and R-curves) is influenced by the width of laser cleaning patterns. Even a 2.5 mm *LC*-treated pattern (P250-T008) could readily improve G_{IIc} by 24%. Increasing the pattern width to 5 mm (P500-T008) slightly improves G_{IIc} by 28%. While, with 10 mm *LC*-treated pattern (P1000-T008), the improvement of G_{IIc} can reach around 60%. This highlights the effectiveness of the patterning strategy is maximized for larger *LC*-treated pattern width. The underlying mechanism behind the large improvement of mode II fracture toughness for large *LC*-treated pattern width was revealed using 3D reconstructed μ-CT image and its corresponding slices. Fig. 12 shows that multiple types of damage were involved in the fracture toughness improvement: crack migration from upper to lower interfaces, and transverse crack growth through the sample width. When the crack reaches the *LC*-treated area, the crack is arrested at the upper interface, which allows the initiation of transverse cracks within the adhesive, and the crack consequently migrates to the lower interface. The crack in the specimen with smaller width of the *LC*-treated pattern (P500-T008) propagates at the lower interface, passing through the treated area, and migrates to the upper interface (with a lower energy). The crack in the specimen with larger width of the *LC*-treated pattern (P1000-T008) propagates within the adhesive,

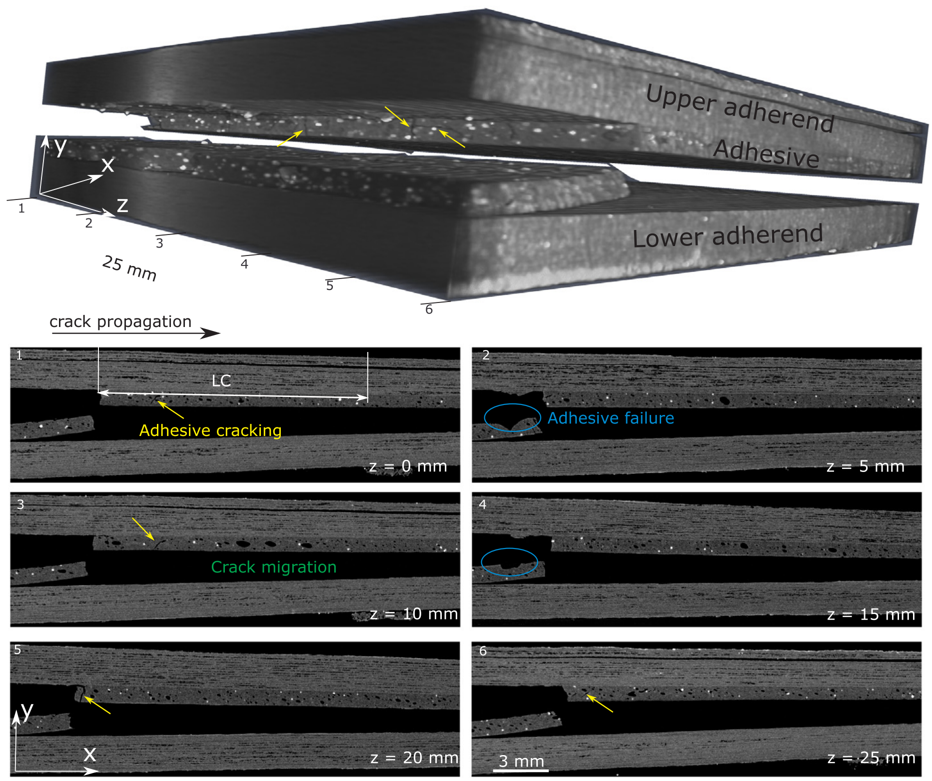

Fig. 12. 3D μ-CT micrographs of P1000-T008 sample (the upper figure) and slices through the sample width (the lower 2D micrographs). (For interpretation of the references to colour in this figure legend, the reader is referred to the web version of this article.)

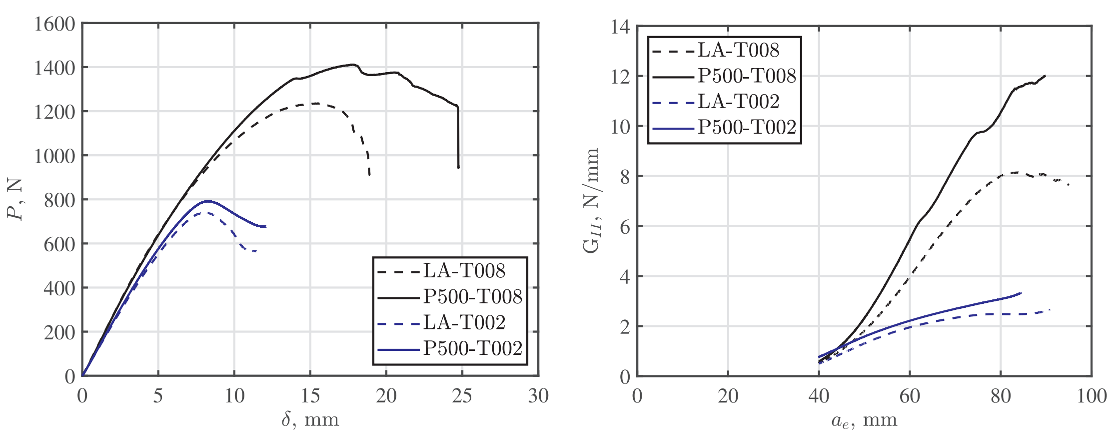

(a) $P - \delta$ (b) G_{II}-a_e

Fig. 13. Effect of *LC* laser treatment on the ENF test response of thin and thick adhesive layers. (For interpretation of the references to colour in this figure legend, the reader is referred to the web version of this article.)

generating a significantly wider crack across the specimen width. The energy required to propagate the crack within the adhesive and across the width consequently improves the fracture toughness.

With the aim of quantifying the effectiveness and the economic value of the proposed patterning strategy, we evaluate the improvement rates achieved in this study together with the improvement rate presented by Moreira et al. [20] for uniformly laser treated samples compared to sand papered ones (G_{IIc} of uniform laser treated adherend/ G_{IIc} of sand papered adherend). Moreira et al. [20] demonstrated ~ 10% improved G_{IIc} for uniform laser treated adherend surface compared to paper sanded ones. In the current study, we reported ~ 60% improvement for laser patterned surface compared to uniform laser treatment. Therefore, we can approximate that a total of ~ 70% G_{IIc} improvement is gained considering our proposed technique compared to sand papered adherends.

4.3. Effect of adhesive thickness

Fig. 13 shows that a thicker adhesive bondline produces a higher fracture toughness than the thinner bondline. The thicker bondline provides a larger fracture process zone, allowing stress redistribution that could reduce the stress concentration at the tip of the propagating crack [26]. In contrast, the fracture process zone in the thinner bondline is very limited, causing the crack to propagate rapidly, thus reaching the failure point earlier than the thicker bondline. Nonetheless, our laser patterning approach was still effective enough to be implemented in a thinner bondline since G_{IIc} can also be improved by 24.9% with a patterning width of 5 mm.

5. Conclusions

Here, we present a novel approach for improving the mode II fracture toughness of secondary bonded carbon/epoxy laminates based on laser patterning of adherend surfaces. We applied laser treatments to the adherend surfaces (that were treated with peel-ply) with different energies resulting in a pattern of smooth (laser ablation, *LA*) and rough (laser cleaning, *LC*) areas. This treatment strategy resulted in a depth difference of surface roughness, which helps to arrest the crack propagation. We performed the ENF test to characterize G_{IIc}, while 3D μ-CT inspection was employed to define different damage mechanisms. The effects of *LC*-treated pattern width (2.5, 5 and 10 mm) and adhesive bondline thickness (0.2 and 0.8 mm) were studied.

Our proposed laser patterning approach improved G_{IIc} by 23.8% for the *LC*-treated width of 2.5 mm compared to the uniform laser ablation treatment. We achieved a further G_{IIc} improvement up to 60% by increasing *LC*-treated width of 10 mm. With the aid of 3D μ-CT, the underlying mechanism behind the improvement was due to the activation of non-local damage mechanisms, namely adhesive cracking, adhesive failure, and crack migration to another interface. The crack that initiated and propagated at the upper interface was arrested by the *LC*-treated pattern. When the crack was arrested, a higher energy was required to propagate the crack within the adhesive. These non-local damage mechanisms were responsible for improving the fracture energy of the adhesive joint under mode II. The proposed approach was found effective for thin and thick adhesive bondlines, which highlighted the approach's applicability for secondary bonded joints in aerospace (thin bondline) and civil (thick bondline) applications.

Author contributions

G.L. supervised the study. G.L. and A.W. conceptualized the study. A.W., R.T. and A.Y. ran experimental tests. A.W. and G.L. performed data curation and formal analysis. All authors participated in writing, reviewing & editing the manuscript.

Declaration of Competing Interest

The authors declare that they have no known competing financial interests or personal relationships that could have appeared to influence the work reported in this paper.

Acknowledgement

This research was funded by King Abdullah University of Science and Technology (KAUST) Office of Sponsored Research (OSR) under award number OSR-2017-CRG6-3388.01.

Appendix A. Supplementary material

Supplementary data associated with this article can be found, in the online version, at https://doi.org/10.1016/j.compositesa.2020.105892.

References

[1] Kruse T. Bonding of CFRP primary aerospace structures: overview on the technology status in the context of the certification boundary conditions adressing needs for development. The 19th international conference on composite materials. 2013. p. 5635–43.
[2] Ageorges C, Ye L, Hou M. Advances in fusion bonding techniques for joining thermoplastic matrix composites: a review. Compos Part A: Appl Sci Manuf 2001;32(6):839–57.
[3] Russell JD. Composites affordability initiative: transitioning advanced aerospace technologies through cost and risk reduction. AMMTIAC Quart 2006;1(3):3–6.
[4] Matthews F, Kilty P, Godwin E. A review of the strength of joints in fibre-reinforced plastics. Part 2. Adhesively bonded joints. Composites 1982;13(1):29–37.
[5] Bardis JD, Kedward KT. Surface preparation effects on mode I testing of adhesively bonded composite joints. J Compos Technol Res 2002;24(1):30–7.
[6] Prolongo S, Gude M, Del Rosario G, Ureña A. Surface pretreatments for composite joints: study of surface profile by SEM image analysis. J Adhes Sci Technol 2010;24(11–12):1855–67.
[7] Holtmannspötter J, Czarnecki J, Wetzel M, Dolderer D, Eisenschink C. The use of peel ply as a method to create reproduceable but contaminated surfaces for structural adhesive bonding of carbon fiber reinforced plastics. J Adhes 2013;89(2):96–110.
[8] Boerio F, Roby B, Dillingham R, Bossi R, Crane R. Effect of grit-blasting on the surface energy of graphite/epoxy composites. J Adhes 2006;82(1):19–37.
[9] Dillingham R, Oakley B. Surface energy and adhesion in composite–composite adhesive bonds. J Adhes 2006;82(4):407–26.
[10] Tserpes K, Peikert G, Floros I. Crack stopping in composite adhesively bonded joints through corrugation. Theoret Appl Fract Mech 2016;83:152–7.
[11] Yukimoto Y, Matsuzaki R, Todoroki A. Mode II interfacial fracture toughness of composite/adhesive interfaces obtained by in-mold surface modification. Int J Adhes Adhes 2014;50:191–8.
[12] Chang P, Mouritz A, Cox B. Properties and failure mechanisms of pinned composite lap joints in monotonic and cyclic tension. Compos Sci Technol 2006;66(13):2163–76.
[13] Nair AB, Sivasubramanian P, Balakrishnan P, Kumar KANA, Sreekala MS. Environmental effects, biodegradation, and life cycle analysis of fully biodegradable green composites. Edited by Sabu Thomas, Kuruvilla Joseph, SK Malhotra; 2014.
[14] Jain LK, Dransfield KA, Mai YW. On the effects of stitching in CFRPs-II. Mode II delamination toughness. Compos Sci Technol 1998;58(6):829–37.
[15] Yudhanto A, Lubineau G, Ventura IA, Watanabe N, Iwahori Y, Hoshi H. Damage characteristics in 3d stitched composites with various stitch parameters under in-plane tension. Compos Part A: Appl Sci Manuf 2015;71:17–31.
[16] Kim J, Baillie C, Poh J, Mai YW. Fracture toughness of CFRP with modified epoxy resin matrices. Compos Sci Technol 1992;43(3):283–97.
[17] Tang LC, Zhang H, Sprenger S, Ye L, Zhang Z. Fracture mechanisms of epoxy-based ternary composites filled with rigid-soft particles. Compos Sci Technol 2012;72(5):558–65.
[18] Löbel T, Holzhüter D, Sinapius M, Hühne C. A hybrid bondline concept for bonded composite joints. Int J Adhes Adhes 2016;68:229–38.
[19] Heide-Jørgensen S, de Freitas ST, Budzik MK. On the fracture behaviour of CFRP bonded joints under mode I loading: Effect of supporting carrier and interface contamination. Compos Sci Technol 2018;160:97–110.
[20] Moreira R, Oliveira V, Silva F, Vilar R, de Moura M. Mode II fracture toughness of carbon–epoxy bonded joints with femtosecond laser treated surfaces. Int J Mech Sci 2018;148:707–13.
[21] Fischer F, Kreling S, Jäschke P, Frauenhofer M, Kracht D, Dilger K. Laser surface pre-treatment of CFRP for adhesive bonding in consideration of the absorption behaviour. J Adhes 2012;88(4–6):350–63.
[22] Botana-Galvín M, Blanco G, González-Rovira L, Rodríguez MA, Botana FJ. Adhesive behaviour of carbon fibre reinforced plastic panels manufactured using woven and unidirectional tape after ultraviolet laser surface treatment. J Compos Mater 2018;52(7):853–65.
[23] Tao R, Alfano M, Lubineau G. In situ analysis of interfacial damage in adhesively bonded composite joints subjected to various surface pretreatments. Compos Part A: Appl Sci Manuf 2019;116:216–23.
[24] Tao R, Alfano M, Lubineau G. Laser-based surface patterning of composite plates for improved secondary adhesive bonding. Compos Part A: Appl Sci Manuf 2018;109:84–94.
[25] O'Brien TK. Composite interlaminar shear fracture toughness, GIIc: Shear measurement or sheer myth? Tech. Rep. NASA TM-110280; NASA Langley Research Center Hampton, VA 23681–0001 and Vehicle Technology Center; 1997.
[26] da Silva LF, De Magalhaes F, Chaves F, De Moura M. Mode II fracture toughness of a brittle and a ductile adhesive as a function of the adhesive thickness. J Adhes 2010;86(9):891–905.
[27] Pérez-Galmés M, Renart J, Sarrado C, Brunner A, Rodríguez-Bellido A. Towards a consensus on mode II adhesive fracture testing: experimental study. Theoret Appl Fract Mech 2018;98:210–9.
[28] Hashemi S, Kinloch AJ, Williams J. The analysis of interlaminar fracture in uniaxial fibre-polymer composites. Proc Roy Soc London A Math Phys Sci 1990;427(1872):173–99.
[29] De Moura M, Campilho R, Gonçalves J. Pure mode II fracture characterization of composite bonded joints. Int J Solids Struct 2009;46(6):1589–95.
[30] Fernandes R, Chousal J, De Moura M, Xavier J. Determination of cohesive laws of composite bonded joints under mode II loading. Compos Part B: Eng 2013;52:269–74.
[31] Yang Q, Thouless M, Ward S. Numerical simulations of adhesively-bonded beams failing with extensive plastic deformation. J Mech Phys Solids 1999;47(6):1337–53.
[32] De Moura M, De Morais A. Equivalent crack based analyses of ENF and ELS tests. Eng Fract Mech 2008;75(9):2584–96.
[33] Campilho RDSG, De Moura M, Ramantani D, Morais J, Domingues J. Tensile behaviour of three-dimensional carbon-epoxy adhesively bonded single-and double-strap repairs. Int J Adhes Adhes 2009;29(6):678–86.
[34] Budzik M, Jumel J, Salem NB, Shanahan M. Instrumented end notched flexure–crack propagation and process zone monitoring Part II: Data reduction and experimental. Int J Solids Struct 2013;50(2):310–9.
[35] Davies P, Sims G, Blackman B, Brunner A, Kageyama K, Hojo M, et al. Comparison of test configurations for the determination of GIIc of unidirectional carbon/epoxy composites, an international round robin. Plast Rubber Compos 1999;28(9):432–7.
[36] Allix O, Ladeveze P, Corigliano A. Damage analysis of interlaminar fracture specimens. Compos Struct 1995;31(1):61–74.
[37] Sorrentino L, Marfia S, Parodo G, Sacco E. Laser treatment surface: an innovative method to increase the adhesive bonding of ENF joints in CFRP, November 2019. Compos Struct February 2020;233:111638.